

Topological Time-series Analysis with Delay-variant Embedding

Hoan Tran Quoc* and Yoshihiko Hasegawa†

Department of Information and Communication Engineering,
Graduate School of Information Science and Technology,
The University of Tokyo, Tokyo 113-8656, Japan

(Dated: December 16, 2022)

Identifying qualitative changes in time-series data provides insights into the dynamics behind these data. Such changes can be detected through topological approaches, which first embed the time-series data into a high-dimensional space using a time-delay parameter and subsequently extract topological features describing the shape of the data from the embedded points. However, the essential topological features extracted at a single time-delay value are not sufficient for evaluating qualitative changes, even when well-chosen time-delay values are used. We propose a delay-variant embedding scheme that constructs the extended topological features by regarding the time delay as a variable parameter, rather than as a single fixed value. This method allows observation of variations in topological features, where time delay serves as an extra dimension in topological-feature space. We theoretically prove that the proposed topological features are robust under noise perturbation of time series. Furthermore, we combine these features with the kernel technique in machine learning to classify general time-series data. We demonstrate the effectiveness of this method in the classification of synthetic noisy biological data and real electrocardiogram data. Our method outperforms that based on a single time-delay value and, surprisingly, achieves the highest classification accuracy on average among standard time-series analysis techniques.

Time-series data undergo qualitative changes, such as transitions from the quiescent state to oscillatory dynamics through bifurcations. The identification of such changes enables a deep understanding of the underlying dynamics, but it is still a challenging problem when the data are subject to noise. In material science, it has been reported that topological features, which indicate the “shape” of the data, can be used to detect qualitative changes, i.e., phase transitions [1, 2] or transitions in morphological and hierarchical structures [3–6]. Since the topology is a qualitative property and is stable under the influence of noise, the topological features of time-series data are expected to reflect qualitative changes in the dynamics. The topological features are constructed through delay embedding, which maps a time series $x(t)$ to m -dimensional points $[x(t), x(t-\tau), \dots, x(t-(m-1)\tau)]$ on the embedded space, where τ is a predefined time-delay parameter and m is the embedding dimension. The embedded points constitute geometric features such as clusters and loops, and the topological features, which monitor the emergence and vanishment of geometric features, can be used to characterize the dynamics of system [7, 8]. The time-delay parameter should reflect the local time-scale of patterns in the time series [9–12]; this indicates that the embedding with a single fixed time-delay parameter does not capture a sufficient amount of information if the time series has multiple patterns with different time-scales. This defect limits the power of topological features for time-series analysis.

In this Letter, we propose a *delay-variant embedding* method that constructs topological features by taking τ as a variable parameter and monitors topological changes in the embedded space over this variable. We theoretically prove the stability of the proposed topological fea-

tures against noise and apply these features to classification of several time-series datasets. In the classification of the oscillatory activity of synthetic noisy biological data, we show that our method outperforms the method based on a single τ value. Surprisingly, in classification of real electrocardiogram data, our approach demonstrates the highest accuracy on average compared with several standard time-series analysis techniques.

To qualitatively evaluate the characteristics of the time series, we apply topological data analysis [13], which is a computational method characterizing the topological features in high-dimensional data. We construct a simplicial-complexes model [14, 15] from the points in the embedded space and obtain the topological information as the number, position, and size of single or multi-dimensional clusters and loops. Given a non-negative scale parameter ε , we build the complex over a set of points if the pairwise distances between them are less than or equal to 2ε . Different ε values result in different complexes and different topological information. If ε is sufficiently small, no connections are created and the resulting simplicial complex is no different than the original points. If we increase ε gradually, the connection between the points appears, and if ε becomes excessively large, all points will be connected with each other and confer no useful information. When we increase parameter ε as a sequence $\varepsilon_1 < \dots < \varepsilon_n$, we obtain a sequence of embedded simplicial complexes called *filtration*.

We use persistent homology theory [16, 17] to study topological features across filtration. A practical way to visualize the result of persistent homology is through the multi-set points in the 2-dimensional *persistence diagram*. In a 2-dimensional persistence diagram denoted as $\text{PD}_l^{(2)}$, each point (b, d) represents an l -dimensional hole (i.e.,

connected components are 0-dimensional; loops or tunnels are 1-dimensional holes, and voids are 2-dimensional holes) that appears at $\varepsilon = b$ (known as the *birth scale*) and disappears at $\varepsilon = d$ (known as the *death scale*) across the filtration. This information encapsulates topological features of the time series after embedding and confers valuable insights into the behavior of dynamical system. For instance, the emergence of oscillation in a time series can appear as the birth of a loop in the embedded space. Using these topological features, the qualitative properties of the time-series data can be captured robustly and efficiently.

For the observed time series $x(t)$, we denote $F_{l,\tau}(x(t))$ as a 2-dimensional persistence diagram calculated for l -dimensional holes from embedded points at time delay τ . We consider τ in a pre-defined set $\mathcal{T} = \{\tau_1, \tau_2, \dots, \tau_K\}$, where $\tau_1 < \tau_2 < \dots < \tau_K$ (with K denoting the set's size) are sampled from the domain of τ . We extend the 2-dimensional persistence diagram to define the 3-dimensional persistence diagram for time series $x(t)$ as $\text{PD}_l^{(3)}(x(t)) = \{(b, d, \tau) \mid (b, d) \in F_{l,\tau}(x(t)), \tau \in \mathcal{T}\}$ where the additional dimension is the time delay τ . Figure 1 shows a schematic of the 3-dimensional persistence diagram where there are different shapes and topological features of embedded points at different τ . As illustrated in the middle panel of Fig. 1, at τ_1 , there are two big loops while at τ_2 or τ_3 , the loops survive for a shorter time, with a different distribution of birth and death scales. Apparently, these kinds of information cannot be obtained with a single fixed τ in the embedding.

Time-series data involve a great deal of noise, which may arise from the measurement or be inherent to the dynamics themselves, and hence the diagrams should be stable against perturbation of the data. To evaluate stability, we need to define a metric structure to compare persistence diagrams. The general metric for 2-dimensional persistence diagrams is the *Wasserstein distance* and we extend this metric to 3-dimensional ones. In a 3-dimensional persistence diagram, all points are located in the half-space above the diagonal plane $\mathcal{W}^{(3)} = \{(b, b, \tau) \mid b, \tau \in \mathbb{R}\}$. Given two 3-dimensional diagrams $Dg_1^{(3)}$ and $Dg_2^{(3)}$, consider all matchings ψ such that a point on $Dg_1^{(3)}$ is matched to a point on $Dg_2^{(3)}$ or to its projected point on $\mathcal{W}^{(3)}$ and vice versa (Fig. 2(a)). The r -Wasserstein distance between $Dg_1^{(3)}$ and $Dg_2^{(3)}$ is defined as $W_r(Dg_1^{(3)}, Dg_2^{(3)}) = \inf_{\psi} \left(\sum_{(\mathbf{p}, \mathbf{q}) \in \psi} \|\mathbf{p} - \mathbf{q}\|_{\infty}^r \right)^{1/r}$, where r is a positive real number and $\|\mathbf{p} - \mathbf{q}\|_{\infty} = \max(|b_1 - b_2|, |d_1 - d_2|, |\tau_1 - \tau_2|)$ if $\mathbf{p} = (b_1, d_1, \tau_1)$, $\mathbf{q} = (b_2, d_2, \tau_2)$. For $r \rightarrow \infty$, the r -Wasserstein distance converges to the *bottleneck distance* $d_B^{(3)}$, which is defined as infimum over all matchings of the longest matched edge

$$d_B^{(3)}(Dg_1^{(3)}, Dg_2^{(3)}) = \inf_{\psi} \max_{(\mathbf{p}, \mathbf{q}) \in \psi} \|\mathbf{p} - \mathbf{q}\|_{\infty}. \quad (1)$$

We show that 3-dimensional persistence diagrams are sta-

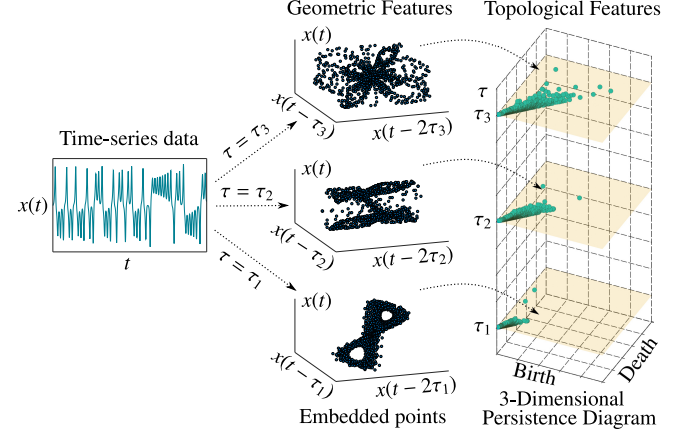


FIG. 1. The time series $x(t)$ is embedded into an m -dimensional space (in this illustration, $m = 3$) through the delay embedding (left panel). Points in the embedded space at different time delays τ have different geometric features, such as clusters and loops (middle panel). Persistent homology [16, 17] extracts topological features such as the emergence (birth scale) and vanishment (death scale) of the geometric features. The birth and death scales at each τ value are represented as points in a 2-dimensional persistence diagram. By observing the variation of topological features where τ serves as an extra dimension, we obtain a 3-dimensional persistence diagram, which can be considered as a typical feature of the time series (right panel).

ble with respect to the bottleneck distance under perturbation applied to the time series. Given two time series $x(t)$ and $y(t)$ with the same length, let $Dg_{(m)}^{(3)}(x)$ and $Dg_{(m)}^{(3)}(y)$ be 3-dimensional persistence diagrams of $x(t)$ and $y(t)$, respectively, calculated at the embedding dimension m . Inspired by the stability properties of 2-dimensional persistence diagrams [18], we prove in [15] the following stability properties of 3-dimensional ones:

$$d_B^{(3)}(Dg_{(m)}^{(3)}(x), Dg_{(m)}^{(3)}(y)) \leq 2\sqrt{m} \|x(t) - y(t)\|_{\infty}, \quad (2)$$

where the distance between $x(t)$ and $y(t)$ is defined as $\|x(t) - y(t)\|_{\infty} = \max_t |x(t) - y(t)|$. When we identify $y(t)$ as the perturbed data obtained by adding noise to $x(t)$, Eq. (2) shows that the bottleneck distance between $Dg_{(m)}^{(3)}(x)$ and $Dg_{(m)}^{(3)}(y)$ is bounded from above by the magnitude of the noise.

In order to use the 3-dimensional persistence diagrams as features for statistical-learning tasks such as classification, we need to define a similarity measure such as a kernel mapping for such diagrams [2, 19, 20]. Since the points close to $\mathcal{W}^{(3)}$ can be neglected as insignificant topological features, they should not influence the computed value of the kernel. Consequently, we define the kernel k_{σ} between two 3-dimensional persistence diagrams $Dg_1^{(3)}$ and $Dg_2^{(3)}$ as $k_{\sigma}(Dg_1^{(3)}, Dg_2^{(3)}) = \frac{1}{\sigma\sqrt{2\pi}} \sum_{\mathbf{p} \in Dg_1^{(3)}, \mathbf{q} \in Dg_2^{(3)}} \left(e^{-\frac{\|\mathbf{p}-\mathbf{q}\|^2}{2\sigma^2}} - e^{-\frac{\|\mathbf{p}-\bar{\mathbf{q}}\|^2}{2\sigma^2}} \right)$, where $\bar{\mathbf{q}}$

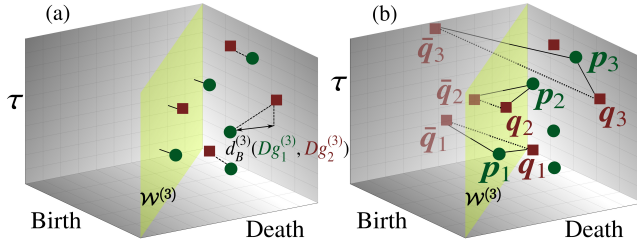


FIG. 2. (a) Bottleneck distance defined in Eq. (1) and the best matching between two diagrams, shown by blue and red points. Some points are matched to their projections on the diagonal plane $\mathcal{W}^{(3)}$. The bottleneck distance is defined as the longest matched edge. (b) Schematic of the kernel between two diagrams shown by blue and red points. Points p_1, q_2 near the diagonal plane in both diagrams have less influence, whereas the pair of points far away from the diagonal plane, i.e., (p_3, q_3) , plays an essential role in the value of the kernel.

is a symmetric point of \mathbf{q} with respect to $\mathcal{W}^{(3)}$, and σ is the kernel's bandwidth. As illustrated in Fig. 2(b), if \mathbf{p} or \mathbf{q} is near the diagonal plane, then $\|\mathbf{p} - \mathbf{q}\| \approx \|\mathbf{p} - \bar{\mathbf{q}}\|$ and the pair (\mathbf{p}, \mathbf{q}) has less influence on the value of the kernel. Based on Ref. [19], we prove that k_σ is a positive-definite kernel and is stable with respect to 1-Wasserstein distance [15]. In the kernel k_σ , we have two parameters: the bandwidth σ and rescale coefficient ξ , which is a scaling parameter introduced to adjust the scale-difference between point-wise distance and time. When we apply k_σ for classification of time series, these parameters affect the classification performance and can be chosen by cross-validation or by a heuristic method [15, 21].

First, we apply the proposed topological features to classify periodic and aperiodic time series from synthetic single-cell data. This is challenging due to the difficulty of discriminating noisy oscillation from mere noisy fluctuation. Traditional methods require detrending of time series, detection of peaks and troughs, or assumption of a mathematical model behind the dynamics [22]. In contrast, our method is an entirely data-based one, focusing on variation of the topological features. We generate synthetic mRNA and protein time-series data from a stochastic model of the *Hes1* genetic oscillator [23, 24] consisting of negative auto-regulation with delay. We use the delayed version of the Gillespie algorithm [25, 26] with the program provided in [22] to generate data from 1,000 cells in both the oscillatory and non-oscillatory parameter regimes [24, 27]. The protein levels were measured every ν ($\nu = 32, 16, 8$) min for 4,096 mins. We normalize the time series to zero-mean and unit-variance, then add the noise with a variance of 10% of a signal at each time point to show the robustness of the method. Figure 3 shows examples of time series and persistence diagrams for the two regimes. In Figs. 3(a) and (d), we show time series generated from (a) non-oscillatory and (d) oscillatory regimes. Figures 3(b) and (e) describe

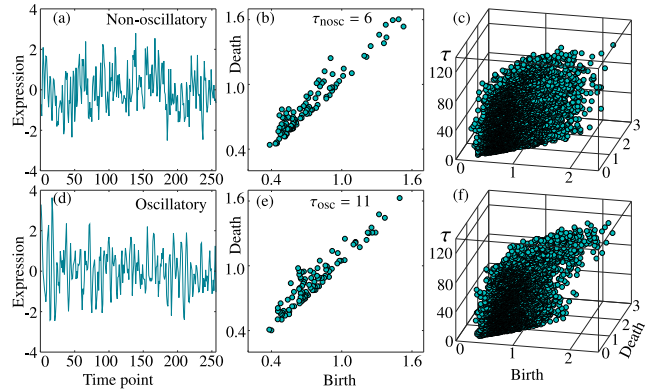


FIG. 3. (a)(d) Examples of two time series with 256 time points generated from (a) the non-oscillatory and (d) oscillatory regime of the *Hes1* model measured every 16 mins. There is almost no difference between the two time series. (b)(e) 2-dimensional persistence diagrams for loop patterns calculated with embedding dimension $m = 3$ and a single τ for (b) non-oscillatory ($\tau = 6$) and (e) oscillatory ($\tau = 11$) time series. There is almost no difference between the two 2-dimensional diagrams. (c)(f) 3-dimensional persistence diagrams for (c) non-oscillatory and (f) oscillatory time series. The topological features of oscillatory data show more pattern variation than do the non-oscillatory data under changes in τ .

2-dimensional persistence diagrams computed from the time series of Figs. 3(a) and (d), respectively. In the same way, Figs. 3(c) and (f) show 3-dimensional persistence diagrams from Figs. 3(a) and (d), respectively. In these examples, it is difficult to distinguish between two regimes using the original time series or 2-dimensional diagrams, whereas there is a distinct pattern for 3-dimensional diagrams since all topological variations are considered when τ changes. In the 3-dimensional diagram of non-oscillatory data, points, which represent loops in the embedded space, are widely distributed along birth and death scales, corresponding to random fluctuation in the time series. In contrast, in the oscillatory data, points are densely distributed along birth and death scales at $\tau = 40-80$; this manifests in the appearance of repeated loop patterns in the embedded space, which indicates periodic patterns in the time series.

We can visually confirm the difference between the extracted topological features using single-delay (single τ) and delay-variant (variant τ) embeddings by projecting the features from the kernel space to 3-dimensional principal components. In the single-delay approach, τ is selected by the mutual-information method [9], and the kernel is computed by the method proposed in [19]. An example of the projection for *Hes1* model data at embedding dimension $m = 3$ and measured interval $\nu = 8$ min is described in Fig. 4 for (a) single-delay and (b) delay-variant methods, where red and green points represent non-oscillatory and oscillatory data, respectively. Although there are many overlapping points in the single-

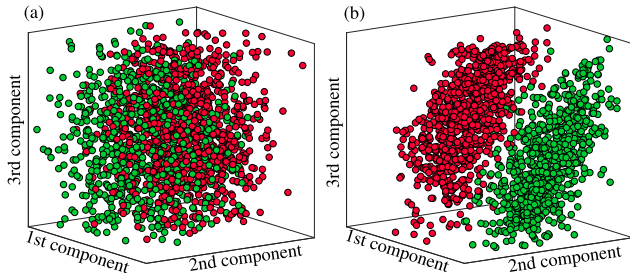


FIG. 4. The projection of features from kernel space to the principal components for (a) single-delay (2-dimensional persistence diagrams) and (b) delay-variant (3-dimensional persistence diagrams) embeddings at dimension $m = 3$ and measured interval $\nu = 8\text{min}$ (red and green points correspond to non-oscillatory and oscillatory data, respectively). While there are many overlapping points in the single-delay method, two regimes can be clearly discriminated in the delay-variant method. Note that the points in the single-delay method cannot be separated, regardless of the angle.

delay method, the delay-variant method shows clear separation between the non-oscillatory and oscillatory cells. Note that the points in the single-delay method cannot be separated, regardless of the angle.

We validate the effectiveness of the proposed topological features by performing classification of Hes1 model data. The data are randomly split 50%-50% into training-test sets. We apply the support vector machine [28] for classification in the kernel space. Figure 5 shows the average classification accuracy over 100 random splits at different embedding dimensions m and different measured intervals ν . The delay-variant method performs significantly better than the single-delay method at all embedding dimensions and all measured intervals. When the measured interval ν increases, the length of the time series becomes shorter, resulting in lower accuracy for both methods; however, the delay-variant method still performs better. Moreover, the accuracy of the delay-variant method does not change from $m = 4$ to $m = 10$, indicating the reliability of the method if the time series is embedded in a space of sufficiently large dimension.

We test the performance of this method in the classification of six real electrocardiogram (ECG) datasets (ECG200, ECG5000, FiveDaysECG, TwoLeadECG, Non-InvasiveFetalECGThorax1, Non-InvasiveFetalECGThorax2) with a train-test split provided in [29]. In single-delay and delay-variant methods, we use a linear combination of kernels at 0-dimensional and 1-dimensional holes [15]. The weights of the combination and the embedding dimension m are selected by cross-validation while m can be increased until the results do not change significantly. We perform a comparison between delay-variant and single-delay methods, and some alternative standard approaches that each of them focuses on similarity in each different

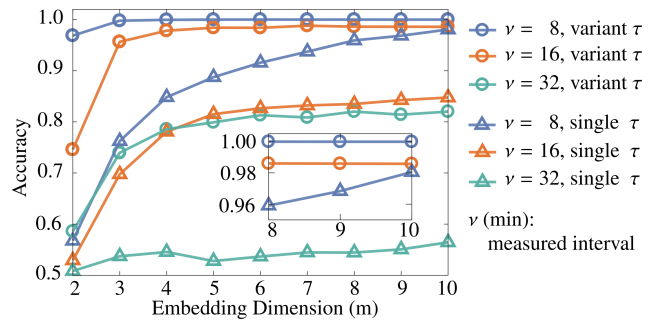


FIG. 5. Average classification accuracy of delay-variant (circle) and single-delay (triangle) methods over 100 random splits of Hes1 model data at different embedding dimensions m and measured intervals $\nu = 8\text{min}$ (blue), 16min (orange), and 32min (green). The inset highlights the results at $m = 8-10$ and Accuracy = 0.96-1.0.

domain. The majority of the research on time-series classification problems has focused on finding appropriate similarity measures for the 1-nearest neighbor (NN) classifier. For similarity in the time domain, we consider the Euclidean (E) or dynamic time wrapping (D) distance. For similarity in the frequency domain or auto-correlation, we consider the power spectrum (PS) and the auto-correlation function (AC). We also examine the elastic ensemble (EE) [30] as a combination of nearest neighbor classifiers using multi distance measures in the time domain. Finally, we compare with learned-shapelets (LS) method in [31], which classifies time series by learning the representative *shapelets* (short discriminant time-series subsequences). We have not implemented these algorithms, but adopt the results from [32, 33]. The test results are presented in Table I wherein the best and second best accuracy scores of each dataset are colored in dark pink and light pink, respectively. The delay-variant method shows better results than the single-delay method for all datasets and outperforms other algorithms on average. For 3 of the 6 datasets, it offers the best results, and it offers the second-best on 3 more. This result suggests that our method can be considered as an effective approach to the classification of time series.

We have demonstrated that the topological features constructed from delay-variant embedding can capture the topological variants of time series when the time-delay value changes. The proposed theory guarantees the stability of the features under perturbation of the data. Our method worked better than other standard methods in the classification of time series. This method can be used to reveal the representative topological features for time series and opens up many possibilities for using topological tools in time-series data analysis.

TABLE I. Classification accuracy (%) with respect to different datasets ECG200, ECG5000, FiveDaysECG (FiveDays), TwoLeadECG (TwoLead), Non-InvasiveFetalECGThorax1 (Thorax1), and Non-InvasiveFetalECGThorax2 (Thorax2). In each dataset, the best and the second-best scores are colored in dark pink and light pink, respectively. The 1-nearest neighbor classifier is abbreviated NN, with Euclidean (E) distance, dynamic time wrapping (D) distance, auto-correlation function (AC), power spectrum (PS), elastic ensemble (EE), and learned-shapelets method (LS).

Data	Delay variant	Delay	Single	NN (E)	NN (D)	NN (AC)	NN (PS)	NN (EE)	NN (LS)
		92.0	78.0	88.0	88.0	82.0	86.0	88.0	88.0
ECG200	93.6	90.4	92.5	92.5	91.0	93.6	93.9	93.2	
ECG5000	99.8	72.7	79.7	79.7	98.1	100.0	82.0	100.0	
FiveDays	99.3	80.9	74.7	86.8	80.4	96.1	97.1	99.6	
TwoLead	91.7	64.2	82.9	82.9	72.1	87.5	84.6	25.9	
Thorax1	93.0	70.9	88.0	87.0	75.2	88.4	91.4	77.0	
Thorax2									

* zoro@biom.t.u-tokyo.ac.jp

† hasegawa@biom.t.u-tokyo.ac.jp

- [1] I. Donato, M. Gori, M. Pettini, G. Petri, S. De Nigris, R. Franzosi, and F. Vaccarino, Phys. Rev. E **93**, 052138 (2016).
- [2] G. Kusano, K. Fukumizu, and Y. Hiraoka, in *Proc. 33th Int. Conf. Machine Learning (ICML)*, Vol. 48 (2016).
- [3] S. Ardanza-Trevijano, I. Zuriguel, R. Arévalo, and D. Maza, Phys. Rev. E **89**, 052212 (2014).
- [4] T. Nakamura, Y. Hiraoka, A. Hirata, E. G. Escolar, and Y. Nishiura, Nanotechnology **26**, 304001 (2015).
- [5] Y. Hiraoka, T. Nakamura, A. Hirata, E. G. Escolar, K. Matsue, and Y. Nishiura, Proc. Natl. Acad. Sci. U.S.A. **113**, 7035 (2016).
- [6] T. Ichinomiya, I. Obayashi, and Y. Hiraoka, Phys. Rev. E **95**, 012504 (2017).
- [7] S. Maletić, Y. Zhao, and M. Rajković, Chaos **26**, 053105 (2016).
- [8] K. Mittal and S. Gupta, Chaos **27**, 051102 (2017).
- [9] A. M. Fraser and H. L. Swinney, Phys. Rev. A **33**, 1134 (1986).
- [10] W. Liebert, K. Pawelzik, and H. G. Schuster, EPL **14**, 521 (1991).

- [11] S. P. Garcia and J. S. Almeida, Phys. Rev. E **71**, 037204 (2005).
- [12] C. Letellier, I. M. Moroz, and R. Gilmore, Phys. Rev. E **78**, 026203 (2008).
- [13] G. Carlsson, Bull. Amer. Math. Soc. **46**, 255 (2009).
- [14] H. Edelsbrunner and J. Harer, *Computational Topology. An Introduction*. (Amer. Math. Soc., 2010).
- [15] See Supplemental Material.
- [16] H. Edelsbrunner, D. Letscher, and A. Zomorodian, Discrete Comput. Geom. **28**, 511 (2002).
- [17] A. Zomorodian and G. Carlsson, Discrete Comput. Geom. **33**, 249 (2005).
- [18] F. Chazal, V. de Silva, and S. Oudot, Geom. Dedicata **173**, 193 (2014).
- [19] J. Reininghaus, S. Huber, U. Bauer, and R. Kwitt, in *2015 IEEE Conf. Computer Vision and Pattern Recognition (CVPR)* (2015).
- [20] M. Carrière, M. Cuturi, and S. Oudot, in *Proc. 34th Int. Conf. Machine Learning (ICML)*, Vol. 70 (2017).
- [21] A. Gretton, K. Fukumizu, C. H. Teo, L. Song, B. Schölkopf, and A. J. Smola, in *Advances in Neural Information Processing Systems 20* (2008).
- [22] N. E. Phillips, C. Manning, N. Papalopulu, and M. Ratnayak, PLOS Comp. Biol. **13**, 1 (2017).
- [23] N. A. Monk, Curr. Biol. **13**, 1409 (2003).
- [24] T. Galla, Phys. Rev. E **80**, 021909 (2009).
- [25] D. T. Gillespie, J. Phys. Chem. **81**, 2340 (1977).
- [26] D. F. Anderson, J. Phys. Chem. **127**, 214107 (2007).
- [27] T. Brett and T. Galla, Phys. Rev. Lett. **110**, 250601 (2013).
- [28] C. M. Bishop, *Pattern Recognition and Machine Learning* (Springer, 2006).
- [29] Y. Chen, E. Keogh, B. Hu, N. Begum, A. Bagnall, A. Mueen, and G. Batista, “The UCR Time Series Classification Archive,” (2015), www.cs.ucr.edu/~eamonn/time_series_data/.
- [30] J. Lines and A. Bagnall, Data Min. Knowl. Disc. **29**, 565 (2014).
- [31] J. Grabocka, N. Schilling, M. Wistuba, and L. Schmidt-Thieme, in *Proc. 20th ACM SIGKDD Int. Conf. Knowledge Discovery and Data Mining* (2014).
- [32] A. Bagnall, J. Lines, A. Bostrom, J. Large, and E. Keogh, Data Min. Knowl. Disc. **31**, 606 (2016).
- [33] A. Bagnall, J. Lines, W. Vickers, and E. Keogh, “The UEA & UCR Time Series Classification Repository,” www.timeseriesclassification.com.

Supplemental Material for “Topological Time-series Analysis with Delay-variant Embedding”

Hoan Tran Quoc and Yoshihiko Hasegawa

This supplementary material describes in detail the calculations introduced in the main text. Equation and figure numbers in this section are prefixed with S (e.g., Eq. (S1) or Fig. S1). Numbers without the prefix (e.g., Eq. (1) or Fig. 1) refer to items in the main text.

1 Topological features from data

We consider the input data as a set P of points in the Euclidean space \mathbb{R}^L . Our main interest is finding the essential topological features, which are considered to be the “shape” of the data. In the main text, topological features are defined as the emergence and vanishment of geometric features such as clusters and loops when considering a sequence of simplicial complexes constructed from points. Here, a simplicial complex is a finite set of simplices where an n -simplex ($n = 0, 1, 2, \dots$) is a fully connected set of $n + 1$ affinely independent points.

To extract the topological features from P , we build a ε -scale Vietoris–Rips complex (denoted as $\text{VR}(P, \varepsilon)$) from a union of L -dimensional hyperspheres of radius ε centered at each point in P . Every collection of $n + 1$ affinely independent points in P forms an n -simplex in $\text{VR}(P, \varepsilon)$ if the pairwise distance between points is less than or equal to 2ε . The complex $\text{VR}(P, \varepsilon)$ gives us the topological information from P associated with radius ε . For example, in Fig. S1(d), there are two loops (called 1-dimensional holes) and one connected component (called a 0-dimensional hole). However, this information depends on how to choose the radius ε . If ε is too small, the complex created by union hyperspheres (Fig. S1(b)) remains almost the same as the discrete points (Fig. S1(a)). If ε is too large, we obtain a trivially connected and overlapped complex without any hole inside it (Fig. S1(f)).

The problem above can be solved by considering not only a single radius, but all choices of radius ε . This yields a *filtration*, which is a sequence of simplicial complexes used to monitor the appearance of holes such as clusters and loops over changing ε . For example, in Fig. S1, we start from $\varepsilon = 0$ (Fig. S1(a)); then we increase ε gradually to see whether the holes appear or disappear at different values of ε . When a hole appears and disappears at radii $\varepsilon = b$ and $\varepsilon = d$, respectively, the hole is characterized by a pair (b, d) , where b , d , and (b, d) are referred to as the *birth scale*, *death scale*, and *persistence pair*, respectively. This persistence pair is calculated for all holes that appear in a filtration.

The persistence pairs, which we use as topological features, are displayed in the Cartesian plane as a 2-dimensional persistence diagram where the birth and death scales appear as the horizontal and vertical coordinates, respectively. In the 2-dimensional persistence diagram, points far from the diagonal generally correspond to robust features, which are persistent over a long time, whereas those near the diagonal are regarded as noise in the data. We provide an exemplary 2-dimensional persistence diagram in Fig. S2, where we consider the appearance and disappearance of loops in a filtration of the Vietoris–Rips complex constructed from points when ε takes the discrete values from the set $\{0, 0.1, 0.2, 0.3, 0.4, 0.5, 0.6\}$. In Fig. S2, there are two persistence pairs $(0.2, 0.4)$ (blue circle) and $(0.3, 0.6)$ (red triangle) which represent the appearance and disappearance of a blue loop (appears at $\varepsilon = 0.2$ then disappears at $\varepsilon = 0.4$) and a red loop (appears at $\varepsilon = 0.3$ then disappears at $\varepsilon = 0.6$) in the filtration, respectively. Please refer to [1] for more details concerning mathematical definitions and computational algorithms.

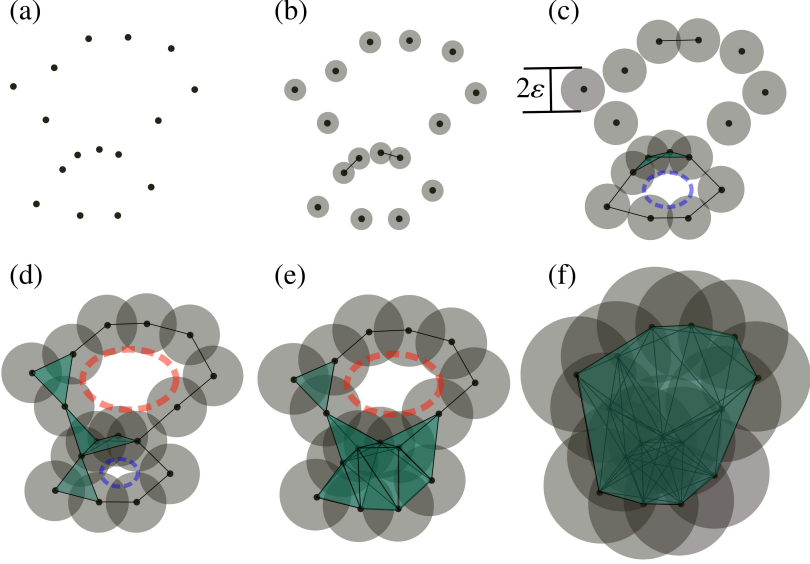


Figure S1: We consider L -dimensional hyperspheres with radius ε centered at each point. From (a) to (f), we increase the radius ε gradually. By increasing ε , holes appear and disappear in the region. The first 1-dimensional hole (blue loop) appears at (c), while the second (red loop) appears at (d). Then at (e), the first hole disappears and finally the second one disappears at (f).

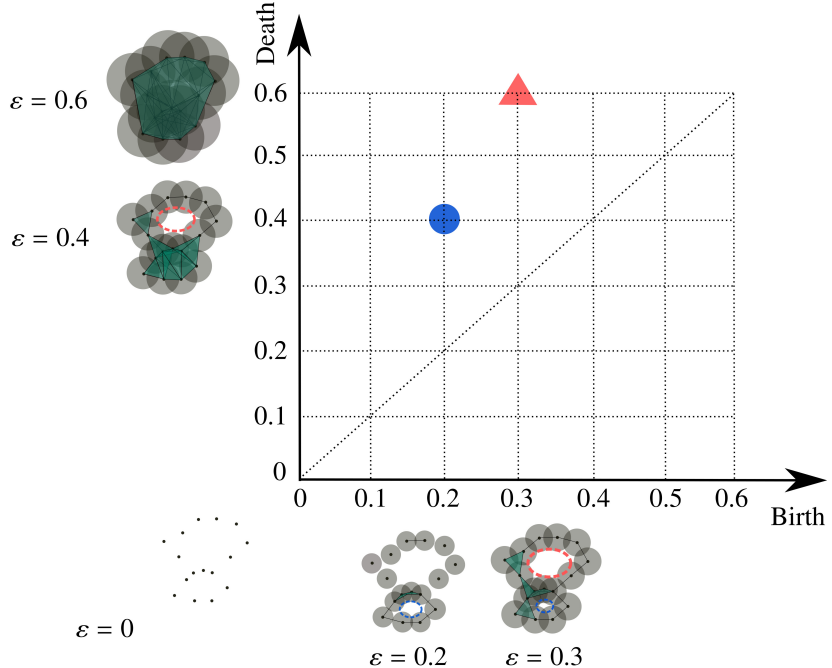


Figure S2: An exemplary 2-dimensional persistence diagram calculated by considering the appearance and disappearance of loops from a filtration of the Vietoris–Rips complex. The radius ε takes the discrete values from the set $\{0, 0.1, 0.2, 0.3, 0.4, 0.5, 0.6\}$. There are two persistence pairs $(0.2, 0.4)$ and $(0.3, 0.6)$, which represent the appearance and disappearance of the blue loop and the red loop, respectively, in the filtration. These persistence pairs are displayed as a blue circle and a red triangle in the Cartesian plane, respectively. The collection of all the persistence pairs in the filtration is a 2-dimensional persistence diagram.

2 Proof of the stability of the 3-dimensional persistence diagram

We define a metric structure to compare the persistence diagrams. In the following definitions, the distance $\|\mathbf{z}\|_\infty$ is defined as $\max\{|z_1|, \dots, |z_n|\}$ for $\mathbf{z} = (z_1, \dots, z_n) \in \mathbb{R}^n$.

The most general metric for 2-dimensional diagrams is the *Wasserstein distance*. In a 2-dimensional persistence diagram, all points are located in the half-plane above the diagonal line $\mathcal{W}^{(2)} = \{(b, b) \mid b \in \mathbb{R}\}$. Given two 2-dimensional diagrams $Dg_1^{(2)}$ and $Dg_2^{(2)}$, consider all matchings γ such that a point on $Dg_1^{(2)}$ is matched to a point on $Dg_2^{(2)}$ or to its projected point on $\mathcal{W}^{(2)}$ and vice versa. The r -Wasserstein distance between $Dg_1^{(2)}$ and $Dg_2^{(2)}$ is defined as $W_r(Dg_1^{(2)}, Dg_2^{(2)}) = \inf_\gamma \left(\sum_{(\mathbf{p}, \mathbf{q}) \in \gamma} \|\mathbf{p} - \mathbf{q}\|_\infty^r \right)^{1/r}$, where r is a positive real number. For $r \rightarrow \infty$, the r -Wasserstein distance for 2-dimensional persistence diagrams converges to the *bottleneck distance* $d_B^{(2)}$ between $Dg_1^{(2)}$ and $Dg_2^{(2)}$, which is defined as infimum over all matchings of the longest matched edge

$$d_B^{(2)}(Dg_1^{(2)}, Dg_2^{(2)}) = \inf_\gamma \max_{(\mathbf{p}, \mathbf{q}) \in \gamma} \|\mathbf{p} - \mathbf{q}\|_\infty. \quad (\text{S1})$$

The bottleneck distance between the 2-dimensional persistence diagrams satisfies the following stability property [2]:

Proposition S1 *Let X and Y be finite sets of points embedded in the Euclidean space \mathbb{R}^n . Denote their 2-dimensional persistent diagrams as $Dg^{(2)}(X)$ and $Dg^{(2)}(Y)$, respectively. Then,*

$$d_B^{(2)}(Dg^{(2)}(X), Dg^{(2)}(Y)) \leq 2d_H(X, Y), \quad (\text{S2})$$

where $d_H(X, Y)$ is the Hausdorff distance given by

$$d_H(X, Y) = \max \left\{ \max_{\mathbf{x} \in X} \min_{\mathbf{y} \in Y} d(\mathbf{x}, \mathbf{y}), \max_{\mathbf{y} \in Y} \min_{\mathbf{x} \in X} d(\mathbf{x}, \mathbf{y}) \right\}, \quad (\text{S3})$$

where $d(\mathbf{x}, \mathbf{y})$ is the Euclidean distance between two points \mathbf{x}, \mathbf{y} in \mathbb{R}^n .

We extend the r -Wasserstein distance to the proposed 3-dimensional persistence diagrams. In a 3-dimensional persistence diagram, all points are located in the half-space above the diagonal plane $\mathcal{W}^{(3)} = \{(b, b, \tau) \mid b, \tau \in \mathbb{R}\}$. Given two 3-dimensional diagrams $Dg_1^{(3)}$ and $Dg_2^{(3)}$, consider all matchings ψ for which a point on $Dg_1^{(3)}$ is matched to a point on $Dg_2^{(3)}$ or to its projected point on $\mathcal{W}^{(3)}$ and vice versa. The r -Wasserstein distance between $Dg_1^{(3)}$ and $Dg_2^{(3)}$ is defined as $W_r(Dg_1^{(3)}, Dg_2^{(3)}) = \inf_\psi \left(\sum_{(\mathbf{p}, \mathbf{q}) \in \psi} \|\mathbf{p} - \mathbf{q}\|_\infty^r \right)^{1/r}$, where r is a positive real number. For $r \rightarrow \infty$, the r -Wasserstein distance for 3-dimensional persistence diagrams converges to the *bottleneck distance* $d_B^{(3)}$ between $Dg_1^{(3)}$ and $Dg_2^{(3)}$

$$d_B^{(3)}(Dg_1^{(3)}, Dg_2^{(3)}) = \inf_\psi \max_{(\mathbf{p}, \mathbf{q}) \in \psi} \|\mathbf{p} - \mathbf{q}\|_\infty. \quad (\text{S4})$$

We prove the next theorem, which leads to the Eq. (2) proposed in the main text.

Theorem S1 *Consider two time series $x(t)$ and $y(t)$ with the same length. Consider τ in a pre-defined set $\mathcal{T} = \{\tau_1, \tau_2, \dots, \tau_K\}$, where $\tau_1 < \tau_2 < \dots < \tau_K$ (with K denoting the set's size) are sampled from the domain of τ . Let $Dg_{(m)}^{(3)}(x)$ and $Dg_{(m)}^{(3)}(y)$ be 3-dimensional persistence diagrams of $x(t)$ and $y(t)$, respectively, calculated at the embedding dimension m . Then we have the following stability properties of 3-dimensional persistence diagrams,*

$$d_B^{(3)}(Dg_{(m)}^{(3)}(x), Dg_{(m)}^{(3)}(y)) \leq 2 \max_{\tau \in \mathcal{T}} d_H(X_{(m)}^\tau, Y_{(m)}^\tau) \leq 2\sqrt{m} \|x(t) - y(t)\|_\infty, \quad (\text{S5})$$

where the distance between $x(t)$ and $y(t)$ is defined as $\|x(t) - y(t)\|_\infty = \max_t |x(t) - y(t)|$, and $X_{(m)}^\tau$ and $Y_{(m)}^\tau$ are the embedded points of $x(t)$ and $y(t)$, respectively, in an embedding space with dimension m and time delay τ .

Proof. For each $\tau \in \mathcal{T}$, we denote the 2-dimensional persistence diagrams calculated from embedded points $X_{(m)}^\tau$ and $Y_{(m)}^\tau$ as $Dg^{(2)}(X_{(m)}^\tau)$ and $Dg^{(2)}(Y_{(m)}^\tau)$, respectively. Let Γ_τ be the set of matchings defined in Eq. (S1) between two 2-dimensional persistence diagrams $Dg^{(2)}(X_{(m)}^\tau)$ and $Dg^{(2)}(Y_{(m)}^\tau)$. For each collection $\Lambda = \{\gamma_1, \gamma_2, \dots, \gamma_K \mid \gamma_i \in \Gamma_{\tau_i}, i = 1, 2, \dots, K\}$, we construct a matching ψ between two 3-dimensional persistence diagrams $Dg_{(m)}^{(3)}(x)$ and $Dg_{(m)}^{(3)}(y)$, such that, for each $\mathbf{p} = (b_1, d_1, \tau) \in Dg_{(m)}^{(3)}(x)$, ψ will map \mathbf{p}

to $\mathbf{q} = (b_2, d_2, \tau) \in Dg_{(m)}^{(3)}(y)$ (and vice versa) such that $(\mathbf{p}_\gamma, \mathbf{q}_\gamma) \in \gamma$, where $\mathbf{p}_\gamma = (b_1, d_1) \in Dg^{(2)}(X_{(m)}^\tau)$ and $\mathbf{q}_\gamma = (b_2, d_2) \in Dg^{(2)}(Y_{(m)}^\tau)$, and $\gamma \in \Lambda \cap \Gamma_\tau$. Let Γ be the set of all matchings ψ constructed this way. From the definition of bottleneck distance, we have the following inequality:

$$d_B^{(3)}(Dg_{(m)}^{(3)}(x), Dg_{(m)}^{(3)}(y)) \leq \inf_{\psi \in \Gamma} \max_{(\mathbf{p}, \mathbf{q}) \in \psi} \|\mathbf{p} - \mathbf{q}\|_\infty. \quad (\text{S6})$$

For $(\mathbf{p}, \mathbf{q}) \in \psi$, we have

$$\|\mathbf{p} - \mathbf{q}\|_\infty = \max\{|b_1 - b_2|, |d_1 - d_2|, |\tau - \tau|\} \quad (\text{S7})$$

$$= \max\{|b_1 - b_2|, |d_1 - d_2|\} = \|\mathbf{p}_\gamma - \mathbf{q}_\gamma\|_\infty, \quad (\text{S8})$$

and Eq. (S6) becomes

$$d_B^{(3)}(Dg_{(m)}^{(3)}(x), Dg_{(m)}^{(3)}(y)) \leq \max_{\tau \in \mathcal{T}} \inf_{\gamma \in \Gamma_\tau} \max_{(\mathbf{p}_\gamma, \mathbf{q}_\gamma) \in \gamma} \|\mathbf{p}_\gamma - \mathbf{q}_\gamma\|_\infty \quad (\text{S9})$$

$$= \max_{\tau \in \mathcal{T}} d_B^{(2)}(Dg^{(2)}(X_{(m)}^\tau), Dg^{(2)}(Y_{(m)}^\tau)). \quad (\text{S10})$$

From Eq. (S10) and Proposition S1, we have the following result:

$$d_B^{(3)}(Dg_{(m)}^{(3)}(x), Dg_{(m)}^{(3)}(y)) \leq \max_{\tau \in \mathcal{T}} d_B^{(2)}(Dg^{(2)}(X_{(m)}^\tau), Dg^{(2)}(Y_{(m)}^\tau)) \leq 2 \max_{\tau \in \mathcal{T}} d_H(X_{(m)}^\tau, Y_{(m)}^\tau). \quad (\text{S11})$$

Next, we prove the second part of the inequality. At each time point t_0 , we consider $\mathcal{X}_{(m)}^\tau(t_0) = (x(t_0), x(t_0 - \tau), \dots, x(t_0 - (m-1)\tau)) \in X_{(m)}^\tau$ and $\mathcal{Y}_{(m)}^\tau(t_0) = (y(t_0), y(t_0 - \tau), \dots, y(t_0 - (m-1)\tau)) \in Y_{(m)}^\tau$. From the definition of Euclidean distance, we have the following result:

$$d(\mathcal{X}_{(m)}^\tau(t_0), \mathcal{Y}_{(m)}^\tau(t_0)) = \sqrt{\sum_{i=0}^{m-1} [x(t_0 + i\tau) - y(t_0 + i\tau)]^2} \leq \sqrt{m} \|x(t) - y(t)\|_\infty. \quad (\text{S12})$$

From Eq. (S12) and the definition of Hausdorff distance, we have the following inequality:

$$d_H(X_{(m)}^\tau, Y_{(m)}^\tau) = \max \left\{ \max_{t_1} \min_{t_2} d(\mathcal{X}_{(m)}^\tau(t_1), \mathcal{Y}_{(m)}^\tau(t_2)), \max_{t_2} \min_{t_1} d(\mathcal{X}_{(m)}^\tau(t_1), \mathcal{Y}_{(m)}^\tau(t_2)) \right\} \quad (\text{S13})$$

$$\leq \max \left\{ \max_{t_1} d(\mathcal{X}_{(m)}^\tau(t_1), \mathcal{Y}_{(m)}^\tau(t_1)), \max_{t_2} d(\mathcal{X}_{(m)}^\tau(t_2), \mathcal{Y}_{(m)}^\tau(t_2)) \right\} \quad (\text{S14})$$

$$\leq \sqrt{m} \|x(t) - y(t)\|_\infty. \quad (\text{S15})$$

The second part of the theorem is obtained by taking the maximum of Eq. (S15) over $\tau \in \mathcal{T}$ and applying it to Eq. (S11).

When we identify $y(t)$ as the perturbed data obtained by adding noise to $x(t)$, Theorem S1 shows that the bottleneck distance between $Dg_{(m)}^{(3)}(x)$ and $Dg_{(m)}^{(3)}(y)$ is bounded from above by the magnitude of the noise.

3 Kernel for the 3-dimensional persistence diagrams

3.1 Proof for the positive-definite property of the kernel

We prove that the proposed kernel for the 3-dimensional persistence diagrams in the main text is positive-definite. Please refer to [3] for the proof for the kernel of the 2-dimensional persistence diagrams.

For each parameter σ and a 3-dimensional persistence diagram $Dg^{(3)}$, we define the following feature mapping $\Phi_\sigma : \mathcal{D}^{(3)} \rightarrow L^2(\Omega)$, where $\mathcal{D}^{(3)}$ is the space of 3-dimensional persistence diagrams, $\Omega = \{\mathbf{x} = (x_1, x_2, x_3) \mid x_1, x_2, x_3 \in \mathbb{R}, x_1 \leq x_2\}$ and $L^2(\Omega)$ is the Hilbert space of square-integrable L^2 -functions defined on the domain Ω :

$$\Phi_\sigma(Dg^{(3)})(\mathbf{x}) = \frac{1}{\sqrt{\kappa}} \sum_{\mathbf{p} \in Dg^{(3)}} e^{-\frac{\|\mathbf{x} - \mathbf{p}\|^2}{\sigma^2}} - e^{-\frac{\|\mathbf{x} - \bar{\mathbf{p}}\|^2}{\sigma^2}}, \quad (\text{S16})$$

where $\bar{\mathbf{p}}$ is a symmetric point of \mathbf{p} with respect to diagonal plane $\mathcal{W}^{(3)}$ on \mathbb{R}^3 and κ is a positive value depending on σ , which we will show later.

We show that the kernel defined in the main text is the inner product of Φ_σ on $L^2(\Omega)$ as

$$k_\sigma(Dg_1^{(3)}, Dg_2^{(3)}) = \langle \Phi_\sigma(Dg_1^{(3)}), \Phi_\sigma(Dg_2^{(3)}) \rangle_{L^2(\Omega)} \quad (\text{S17})$$

$$= \int_{\Omega} \Phi_\sigma(Dg_1^{(3)})(\mathbf{x}) \Phi_\sigma(Dg_2^{(3)})(\mathbf{x}) d\mathbf{x}. \quad (\text{S18})$$

We extend the domain of function $\Phi_\sigma(Dg^{(3)})(\mathbf{x})$ from Ω to \mathbb{R}^3 to obtain a function that is symmetric with respect to the diagonal plane $\mathcal{W}^{(3)}$ (because $\|\mathbf{x} - \mathbf{p}\| = \|\bar{\mathbf{x}} - \bar{\mathbf{p}}\|$ and $\|\mathbf{x} - \bar{\mathbf{p}}\| = \|\bar{\mathbf{x}} - \mathbf{p}\|$). Then we have

$$\int_{\Omega^{(3)}} \Phi_\sigma(Dg_1^{(3)})(\mathbf{x}) \Phi_\sigma(Dg_2^{(3)})(\mathbf{x}) d\mathbf{x} = \frac{1}{2} \int_{\mathbb{R}^3} \Phi_\sigma(Dg_1^{(3)})(\mathbf{x}) \Phi_\sigma(Dg_2^{(3)})(\mathbf{x}) d\mathbf{x} \quad (\text{S19})$$

$$= \frac{1}{2\kappa} \sum_{\mathbf{p} \in Dg_1^{(3)}} \sum_{\mathbf{q} \in Dg_2^{(3)}} [A(\mathbf{p}, \mathbf{q}) + A(\bar{\mathbf{p}}, \bar{\mathbf{q}}) - A(\bar{\mathbf{p}}, \mathbf{q}) - A(\mathbf{p}, \bar{\mathbf{q}})], \quad (\text{S20})$$

where $A(\mathbf{c}, \mathbf{d})$ is defined as

$$A(\mathbf{c}, \mathbf{d}) = \int_{\mathbb{R}^3} e^{-\frac{\|\mathbf{x} - \mathbf{c}\|^2 + \|\mathbf{x} - \mathbf{d}\|^2}{\sigma^2}} d\mathbf{x} = \int_{\mathbb{R}^3} e^{-\frac{\|\mathbf{x} - (\mathbf{c} - \mathbf{d})\|^2 + \|\mathbf{x}\|^2}{\sigma^2}} d\mathbf{x} = \frac{\sigma^3 (2\pi)^{3/2}}{8} e^{-\frac{\|\mathbf{c} - \mathbf{d}\|^2}{2\sigma^2}}. \quad (\text{S21})$$

Here, $\mathbf{c}, \mathbf{d} \in \mathbb{R}^3$. From Eqs. (S20) and (S21) we have

$$k_\sigma(Dg_1^{(3)}, Dg_2^{(3)}) = \frac{\sigma^3 (2\pi)^{3/2}}{16\kappa} \sum_{\mathbf{p} \in Dg_1^{(3)}} \sum_{\mathbf{q} \in Dg_2^{(3)}} \left(e^{-\frac{\|\mathbf{p} - \mathbf{q}\|^2}{2\sigma^2}} + e^{-\frac{\|\bar{\mathbf{p}} - \bar{\mathbf{q}}\|^2}{2\sigma^2}} - e^{-\frac{\|\bar{\mathbf{p}} - \mathbf{q}\|^2}{2\sigma^2}} - e^{-\frac{\|\mathbf{p} - \bar{\mathbf{q}}\|^2}{2\sigma^2}} \right). \quad (\text{S22})$$

Since $\|\mathbf{p} - \mathbf{q}\|^2 = \|\bar{\mathbf{p}} - \bar{\mathbf{q}}\|^2$, $\|\bar{\mathbf{p}} - \mathbf{q}\|^2 = \|\mathbf{p} - \bar{\mathbf{q}}\|^2$, we have the closed form of the kernel as shown in the main text:

$$k_\sigma(Dg_1^{(3)}, Dg_2^{(3)}) = \frac{1}{\sigma\sqrt{2\pi}} \sum_{\mathbf{p} \in Dg_1^{(3)}} \sum_{\mathbf{q} \in Dg_2^{(3)}} e^{-\frac{\|\mathbf{p} - \mathbf{q}\|^2}{2\sigma^2}} - e^{-\frac{\|\mathbf{p} - \bar{\mathbf{q}}\|^2}{2\sigma^2}}, \quad (\text{S23})$$

where $\kappa = \frac{\pi^2 \sigma^4}{2}$.

The kernel is positive-definite due to the inner-product nature of the feature mapping. Consider the 3-dimensional persistence diagrams $Dg_1^{(3)}, Dg_2^{(3)}, \dots, Dg_N^{(3)}$ of the l -dimensional holes that are needed to compute the kernel. The Gram matrix for these diagrams is defined as $\mathbf{K}_{N \times N}^{(l)} = [k_{ij}]$, whose element k_{ij} is $k_{ij} = k_\sigma(Dg_i^{(3)}, Dg_j^{(3)})$ with $i = 1, 2, \dots, N$ and $j = 1, 2, \dots, N$.

3.2 Selecting parameters for the kernel

We denote the sets of time-delay values used to compute $Dg_1^{(3)}$ and $Dg_2^{(3)}$ as \mathcal{T}_1 and \mathcal{T}_2 , respectively. We multiply τ by a rescale coefficient ξ , which is a scaling parameter used to adjust the scale-difference between point-wise distance and time. For each τ , we use the notation $Dg_{1,(\tau)}^{(2)} = \{\mathbf{p}_\tau = (b, d) \mid \mathbf{p} = (b, d, \tau) \in Dg_1^{(3)}\}$, with $Dg_{2,(\tau)}^{(2)}$ having a similar meaning. Then, Eq. (S23) becomes

$$k_\sigma(Dg_1^{(3)}, Dg_2^{(3)}) = \frac{1}{\sigma\sqrt{2\pi}} \sum_{\tau_1 \in \mathcal{T}_1} \sum_{\tau_2 \in \mathcal{T}_2} e^{-\frac{\xi^2 |\tau_1 - \tau_2|^2}{2\sigma^2}} \sum_{\substack{\mathbf{p}^{(2)} \in Dg_{1,(\tau_1)}^{(2)} \\ \mathbf{q}^{(2)} \in Dg_{2,(\tau_2)}^{(2)}}} e^{-\frac{\|\mathbf{p}^{(2)} - \mathbf{q}^{(2)}\|^2}{2\sigma^2}} - e^{-\frac{\|\mathbf{p}^{(2)} - \bar{\mathbf{q}}^{(2)}\|^2}{2\sigma^2}}, \quad (\text{S24})$$

where $\bar{\mathbf{q}}^{(2)}$ is a symmetric point of $\mathbf{q}^{(2)}$ with respect to the diagonal line $\mathcal{W}^{(2)}$ on \mathbb{R}^2 .

In time-series classification experiments, we compute the kernel by taking time-delay values as discrete values with sampling interval 1 and set the rescaling coefficient to $\xi = \sigma$. The selection of kernel bandwidth σ can be chosen by cross-validation; however, as proposed in [4], we present here a heuristic way to select σ . Consider the 3-dimensional persistence diagrams $Dg_1^{(3)}, Dg_2^{(3)}, \dots, Dg_N^{(3)}$ that are required to compute the kernel. We denote $\sigma_s^2 = \text{median}\{(b_i - b_j)^2 + (d_i - d_j)^2 \mid (b_i, d_i, \tau_i), (b_j, d_j, \tau_j) \in Dg_s^{(3)}\}$ with $s = 1, 2, \dots, N$. In our time-series classification experiments, σ is set as $\sigma^2 = \frac{1}{2} \text{median}\{\sigma_s^2 \mid s = 1, \dots, N\}$, such that $2\sigma^2$ takes values close to many $(b_i - b_j)^2 + (d_i - d_j)^2$ values.

3.3 Using kernels with holes of multiple dimensions

For all l -dimensional holes, we obtain the persistence diagrams and compute their kernels as k_{σ_l} , where σ_l is the bandwidth of this kernel. To use persistence diagrams for different dimensions of holes, we can combine the kernels at various dimensions through linear combinations. In our time-series classification experiments, we only consider the topological features of 0-dimensional holes (connected components or clusters) and 1-dimensional holes (loops). Thus, the combined Gram matrix of N data can be defined as

$$\mathbf{K}_{N \times N} = \alpha_0 \mathbf{K}_{N \times N}^{(0)} + \alpha_1 \mathbf{K}_{N \times N}^{(1)}, \quad (\text{S25})$$

where $0 \leq \alpha_0, \alpha_1 \leq 1$, $\alpha_0 + \alpha_1 = 1$, and $\mathbf{K}_{N \times N}^{(0)}$ and $\mathbf{K}_{N \times N}^{(1)}$ are the Gram matrices of N persistence diagrams at the 0-dimensional and 1-dimensional holes, respectively. In our time-series classification experiments, we choose α_0 from $\{0, 0.0001, 0.0002, 0.0005, 0.001, 0.002, 0.005, 0.01, 0.02, 0.05, 0.1, 0.2, 0.5, 1.0\}$ by cross-validation.

3.4 Proof of the stability of the kernel

Based on [3], we prove that the kernel k_σ is stable with respect to 1-Wasserstein distance. We need to prove that there is a positive constant C such that $d_{k_\sigma}(Dg_1^{(3)}, Dg_2^{(3)}) \leq CW_1(Dg_1^{(3)}, Dg_2^{(3)})$, where $d_{k_\sigma}(Dg_1^{(3)}, Dg_2^{(3)})$ is the squared distance in the kernel space between $Dg_1^{(3)}$ and $Dg_2^{(3)}$ defined as

$$d_{k_\sigma}(Dg_1^{(3)}, Dg_2^{(3)}) = \|\Phi_\sigma(Dg_1^{(3)}) - \Phi_\sigma(Dg_2^{(3)})\|_{L^2(\Omega)}, \quad (\text{S26})$$

where $\|\Psi\|_{L^2(\Omega)}$ is the L^2 -norm of function $\Psi \in L^2(\Omega)$, defined as $\|\Psi\|_{L^2(\Omega)} = (\int_{\Omega} \Psi(\mathbf{x})^2 d\mathbf{x})^{1/2}$.

Since the numbers of points in $Dg_1^{(3)}$ and $Dg_2^{(3)}$ are finite, there exists a best matching ψ in the definition of 1-Wasserstein distance between $Dg_1^{(3)}$ and $Dg_2^{(3)}$ that satisfies $W_1(Dg_1^{(3)}, Dg_2^{(3)}) = \sum_{(\mathbf{p}, \mathbf{q}) \in \psi} \|\mathbf{p} - \mathbf{q}\|_\infty$. We use the notation $f_{\mathbf{a}}(\mathbf{x}) = \frac{\sqrt{2}}{\pi\sigma^2} e^{-\frac{\|\mathbf{x}-\mathbf{a}\|^2}{\sigma^2}}$ for $\mathbf{a} \in \mathbb{R}^3$; then, $\Phi_\sigma(Dg_1^{(3)})(\mathbf{x}) = \sum_{\mathbf{p} \in Dg_1^{(3)}} f_{\mathbf{p}}(\mathbf{x}) - f_{\bar{\mathbf{p}}}(\mathbf{x})$ and $\Phi_\sigma(Dg_2^{(3)})(\mathbf{x}) = \sum_{\mathbf{q} \in Dg_2^{(3)}} f_{\mathbf{q}}(\mathbf{x}) - f_{\bar{\mathbf{q}}}(\mathbf{x})$. If $(\mathbf{p}, \mathbf{q}) \in \psi$ and \mathbf{p} (or \mathbf{q}) is the projected point on the diagonal plane $\mathcal{W}^{(3)}$, then $f_{\mathbf{p}}(\mathbf{x}) - f_{\bar{\mathbf{p}}}(\mathbf{x}) = 0$ (or $f_{\mathbf{q}}(\mathbf{x}) - f_{\bar{\mathbf{q}}}(\mathbf{x}) = 0$). Consequently, we have

$$\Phi_\sigma(Dg_1^{(3)})(\mathbf{x}) - \Phi_\sigma(Dg_2^{(3)})(\mathbf{x}) = \sum_{\mathbf{p} \in Dg_1^{(3)}} [f_{\mathbf{p}}(\mathbf{x}) - f_{\bar{\mathbf{p}}}(\mathbf{x})] - \sum_{\mathbf{q} \in Dg_2^{(3)}} [f_{\mathbf{q}}(\mathbf{x}) - f_{\bar{\mathbf{q}}}(\mathbf{x})] \quad (\text{S27})$$

$$= \sum_{(\mathbf{p}, \mathbf{q}) \in \psi} (f_{\mathbf{p}}(\mathbf{x}) - f_{\bar{\mathbf{p}}}(\mathbf{x})) - (f_{\mathbf{q}}(\mathbf{x}) - f_{\bar{\mathbf{q}}}(\mathbf{x})). \quad (\text{S28})$$

Since Eq. (S21), we have

$$\|f_{\mathbf{p}} - f_{\mathbf{q}}\|_{L^2(\mathbb{R}^3)} = \frac{\sqrt{2}}{\pi\sigma^2} \sqrt{A(\mathbf{p}, \mathbf{p}) + A(\mathbf{q}, \mathbf{q}) - 2A(\mathbf{p}, \mathbf{q})} = \frac{1}{\sqrt{\sigma}} \left(\frac{2}{\pi}\right)^{1/4} \sqrt{1 - e^{-\frac{\|\mathbf{p} - \mathbf{q}\|^2}{2\sigma^2}}}; \quad (\text{S29})$$

then

$$\|\Phi_\sigma(Dg_1^{(3)}) - \Phi_\sigma(Dg_2^{(3)})\|_{L^2(\Omega)} = \left\| \sum_{(\mathbf{p}, \mathbf{q}) \in \psi} (f_{\mathbf{p}} - f_{\bar{\mathbf{p}}}) - (f_{\mathbf{q}} - f_{\bar{\mathbf{q}}}) \right\|_{L^2(\Omega)} \quad (\text{S30})$$

$$\leq \left\| \sum_{(\mathbf{p}, \mathbf{q}) \in \psi} (f_{\mathbf{p}} - f_{\bar{\mathbf{p}}}) - (f_{\mathbf{q}} - f_{\bar{\mathbf{q}}}) \right\|_{L^2(\mathbb{R}^3)} \quad (\text{S31})$$

$$\leq \sum_{(\mathbf{p}, \mathbf{q}) \in \psi} \|f_{\mathbf{p}} - f_{\mathbf{q}}\|_{L^2(\mathbb{R}^3)} + \|f_{\bar{\mathbf{p}}} - f_{\bar{\mathbf{q}}}\|_{L^2(\mathbb{R}^3)} \quad (\text{S32})$$

$$= 2 \sum_{(\mathbf{p}, \mathbf{q}) \in \psi} \|f_{\mathbf{p}} - f_{\mathbf{q}}\|_{L^2(\mathbb{R}^3)} \quad (\text{S33})$$

$$= \frac{2}{\sqrt{\sigma}} \left(\frac{2}{\pi}\right)^{1/4} \sum_{(\mathbf{p}, \mathbf{q}) \in \psi} \sqrt{1 - e^{-\frac{\|\mathbf{p} - \mathbf{q}\|^2}{2\sigma^2}}} \quad (\text{S34})$$

$$\leq \frac{1}{\sigma\sqrt{\sigma}} \left(\frac{8}{\pi}\right)^{1/4} \sum_{(\mathbf{p}, \mathbf{q}) \in \psi} \|\mathbf{p} - \mathbf{q}\| \leq \frac{3}{\sigma\sqrt{\sigma}} \left(\frac{8}{\pi}\right)^{1/4} \sum_{(\mathbf{p}, \mathbf{q}) \in \psi} \|\mathbf{p} - \mathbf{q}\|_\infty. \quad (\text{S35})$$

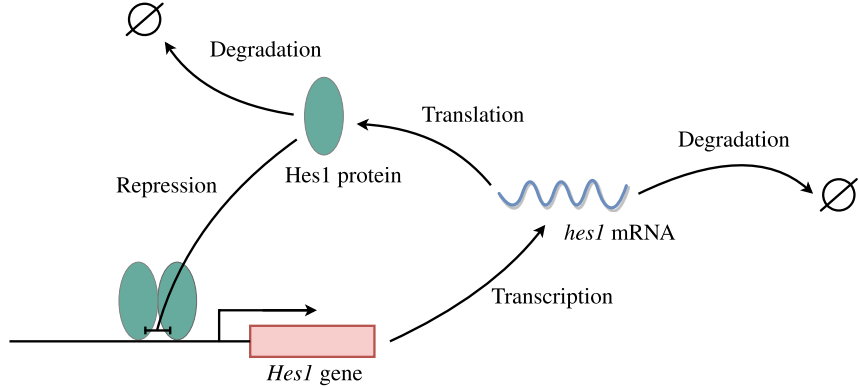


Figure S3: Schematic of the Hes1 regulatory model. mRNA molecules are produced by the transcription of DNA. The production of Hes1 protein occurs by translation of *hes1* mRNA with delay time ζ . The Hes1 protein represses its own expression by directly binding to its promoter as negative feedback.

The transformation from Eq. (S31) to Eq. (S32) is due to the Minkowski inequality and the transformation from Eq. (S34) to Eq. (S35) is due to the inequality $1 - e^{-\eta} \leq \eta$ with $\eta \in \mathbb{R}, \eta \geq 0$. Equation (S35) shows the stability of the proposed kernel with respect to the 1-Wasserstein distance.

4 Synthetic data

We generate data from Hes1 regulatory model, which is a stochastic model of a *Hes1* genetic oscillator which consists of negative auto-regulation with delay [6, 7]. The network topology of the model is illustrated in Fig. S3. The model describes the concentrations and interactions of two types of particles: *hes1* mRNA molecules, denoted by M , and Hes1 protein molecules, denoted by P . The stochastic dynamics are defined by the following four reactions:



The degradations of mRNA and protein are described in reactions (S36) and (S37), respectively, where the rates of these degradation are μ_m and μ_p , respectively. mRNA molecules are translated into protein via reaction (S38) by the translation-rate parameter β_p . The final reaction, (S39) with a double arrow describes the transcription process for producing mRNA which is accompanied by time delay. The rate of *hes1* mRNA production depends on the concentration of Hes1 protein molecules through a negative-feedback mechanism, as described by the function $g(n_p) = \beta_m \left[1 + [n_p/(P_0 \Theta)]^h \right]^{-1}$, where n_p is the number of protein molecules in the system, β_m , P_0 , and h are constants, and Θ is the size of the system. This transcription process is associated with a time delay ζ drawn from a distribution $K(\zeta)$; that is, the protein concentration at time $t - \zeta$ only affects the production of mRNA at time t . The data is simulated using the delayed version of the Gillespie algorithm [8, 9]. The simulation program is provided in [5] and we generate data from 1,000 cells in both oscillatory and non-oscillatory parameter regimes [7, 10]. In the simulations, the protein levels were measured every ν ($\nu = 32, 16, 8, 4, 2, 1$) min for 4,096 mins. The measurements start at $t = 5,000$ min for the system to equilibrate. We add the noise with a variance of 10% of a signal at each time point to show the robustness of the method.

To confirm that the parameter regimes used in the simulation are oscillatory or non-oscillatory, we apply the Fourier transform to the generated time-series data at the measured interval $\nu = 1$ min. Although the power spectrum cannot be used to distinguish two regimes with individual time series, the average power spectrum of 1,000 data points in each parameter regime shows clear oscillatory or non-oscillatory behavior (Fig. S4). In the oscillatory regime, there is a clear peak at a frequency of 0.5 hours $^{-1}$, whereas the average power spectrum in the non-oscillatory regime shows no peak.

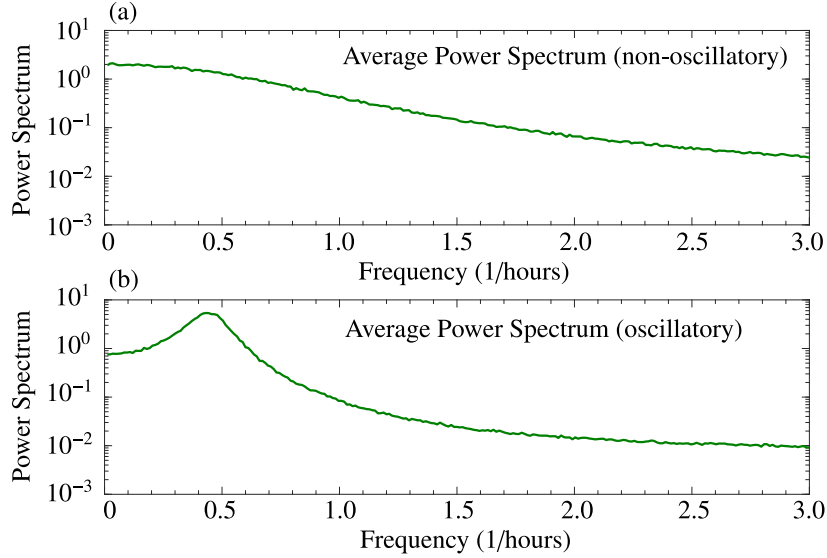


Figure S4: Average power spectra of the protein concentrations calculated from Gillespie simulation of 1,000 independent non-oscillating data points (a) and 1,000 oscillating data points (b). The measurements start at $t = 5,000\text{min}$ for the system to equilibrate. Parameters for (a) are $P_0 = 300, h = 1, \zeta = 0, \beta_m = \beta_p = 1, \mu_m = \mu_p = 0.07, \Theta = 20$, and for (b) are $P_0 = 100, h = 3, \zeta = 18, \beta_m = \beta_p = 1, \mu_m = \mu_p = 0.03, \Theta = 20$. The time series are generated with measurements every 1 min over a period of $t = 9,096\text{min}$.

References

- [1] H. Edelsbrunner, J. Harer. Computational topology. An introduction. Amer. Math. Soc., 2010.
- [2] F. Chazal, V. de Silva and S. Oudot. Persistence stability for geometric complexes. *Geometriae Dedicata*, 173(1):193–214, 2014.
- [3] J. Reininghaus, S. Huber, U. Bauer and R. Kwitt. A stable multi-scale kernel for topological machine learning. *2015 IEEE Conf. Computer Vision and Pattern Recognition (CVPR)*, 2015.
- [4] A. Gretton, K. Fukumizu, C. H. Teo, L. Song, B. Schölkopf and A. J. Smola. A kernel statistical test of independence. *Advances in Neural Information Processing Systems 20*, 2008.
- [5] N. E. Phillips, C. Manning, N. Papalopulu, and M. Rattray. Identifying stochastic oscillations in single-cell live imaging time series using Gaussian processes. *PLOS Comp. Biol.*, 13(5), 2017.
- [6] N. A. Monk. Oscillatory expression of Hes1, p53, and NF- κ B driven by transcriptional time delays. *Curr. Biol.*, 13(16):1409–1413, 2003.
- [7] T. Galla. Intrinsic fluctuations in stochastic delay systems: Theoretical description and application to a simple model of gene regulation. *Phys. Rev. E*, 80(2):021909, 2009.
- [8] D. T. Gillespie. Exact stochastic simulation of coupled chemical reactions. *J. Phys. Chem.*, 81(25):2340–2361, 1977.
- [9] D. F. Anderson. A modified next reaction method for simulating chemical systems with time dependent propensities and delays. *J. Phys. Chem.*, 127(21):214107, 2007.
- [10] T. Brett and T. Galla. Stochastic processes with distributed delays: chemical Langevin equation and linear-noise approximation. *Phys. Rev. Lett.*, 110(25):250601, 2013.